Annales Univ. Sci. Budapest., Sect. Comp. 58 (2025) 209–230

HYBRID OSEM-PDHG RECONSTRUCTION FOR SPECT WITH NON-SMOOTH TOTAL VARIATION REGULARIZATION

Dávid Légrády, Ákos Rábely and Ádám Zlehovszky
(Budapest, Hungary)

Communicated by László Szili
(Received 29 May 2025; accepted 25 July 2025)

Abstract. We propose a novel hybrid reconstruction method for SPECT imaging that integrates the OSEM algorithm with Condat's extension of the PDHG method, enabling the usage of non-smooth TV functional as a prior. Unlike traditional OSL scheme that requires smoothed version of TV, our approach directly incorporates non-smooth TV. To ensure spatially uniform regularization strength, even when attenuation is modeled, we introduce a sensitivity-based compensation strategy in the PDHG update step. This adjustment improves regularization consistency and simplifies the selection of regularization parameters. We evaluate the method using Monte Carlo simulations of a Jaszczak phantom under varying noise conditions. The proposed OSEM-PDHG framework outperforms OSL-TV in terms of PSNR, SSIM, and noise suppression, particularly in low-SNR scenarios. While increased regularization reduces contrast in small structures such as cold rods, the method achieves significantly improved image quality without compromising stability. Our results suggest that this framework is a robust and flexible alternative for noise-aware SPECT reconstruction.

1. Introduction

Single photon emission computed tomography (SPECT) is a widely utilized nuclear imaging modality used in diagnostic imaging. During image acquisition

Key words and phrases: Emission tomography, reconstruction, Primal-Dual Methods.
2010 Mathematics Subject Classification: 68U10.
The current work is prepared with the professional support of the Doctoral Student Scholarship of the Co-operative Doctoral Program of the Ministry of Culture and Innovation financed by the National Research, Development, and Innovation Fund.
https://doi.org/10.71352/ac.58.250725
First published online: 31 July 2025

a single- or multi-headed, typically rotating gamma camera detects γ-photons that escape the field of view (FOV) of the scan based on their incoming direction and energy. This acquisition process can be modelled mathematically with a linear operator that maps from the activity distribution within FOV of the scan to the corresponding measurement data. The linear operator commonly referred to *forward-projection*; it can account for various physical properties of the detector system (e.g. spatial and energy resolution, system sensitivity) as well as the underlying physics of the imaging process (e.g. attenuation, radioactive decay). The adjoint of the operator is known as the *back-projection*.

In SPECT imaging, the objective of reconstruction is to estimate the spatial distribution of radioactive isotope activity within the detector system's FOV, based on measurements acquired during the scan. Due to the inherently stochastic nature of radioactive decay, the resulting measurement data are affected by noise. Consequently, SPECT reconstruction is formulated as a statistical inverse problem, wherein the unknown activity distribution is mapped to the measured data via the forward-projection operator and subsequently inferred from noisy observations.

The simplest model of the SPECT forward-projection operator is the Radon transform. In this case, the reconstruction can be performed with the inverse Radon transform, typically implemented through the filtered back-projection (FBP) method. This analytical approach requires only a single computation step, making it highly efficient. However, the inverse Radon transform is an unbounded linear operator, rendering it particularly sensitive to measurement noise. Moreover, if the forward-projection incorporates additional physical process, such as as attenuation, spatial resolution, an explicit analytic inverse may no longer exists or is unknown, limiting the applicability of FBP in such cases.

To address the limitations of FBP, iterative reconstruction methods are commonly employed. During SPECT scan, detected photon hits are counted within finite-sized rectangular regions (pixels) of the detector system. It is generally assumed that the number of detected events in each pixel follows independent Poisson distributions, with parameters determined by forward-projection of underlying activity distribution within the FOV of the SPECT scan. Most iterative reconstruction algorithms aim to recover the activity distribution that maximizes the likelihood of the observed measurements under this model.

The maximum likelihood expectation maximization (MLEM) algorithm introduced in [5], is commonly used to obtain a maximum likelihood (ML) estimate of the activity distribution. It operates by alternating between an expectation and a maximization step. In the expectation step, the expected value of complete-data log-likelihood is computed, conditioned on the current estimate of the latent variables. In the maximization step, this conditioned expectation is maximized to update the estimate. While MLEM was originally proposed for positron emission tomography (PET) reconstruction in [15], the mathematical model of SPECT and PET reconstruction is the same, they only differ in the

forward-projector operator. For SPECT reconstruction, both steps are computationally efficient, as they primarily involve applications of the forward- and backward-projection operators. In [10] the authors showed that MLEM can also be interpreted as a diagonally preconditioned gradient ascent method applied to the log-likelihood.

In MLEM-based reconstruction, the majority of computation effort is devoted to the application of forward- and backward-projection operators. The overall runtime can be significantly reduced by partitioning the measurement data into subsets and using only a single subset for calculating the the update of the current estimate of the activity distribution. This strategy underlies the ordered subset expectation maximization (OSEM) algorithm, introduced in [7], which achieves substantial acceleration while maintaining reconstruction quality. While OSEM converges more rapidly, than MLEM in practice, it does not guarantee monotonic increase in the likelihood function and its convergence properties are more complex.

A common drawback of iterative reconstruction methods is the progressive amplification of noise with increasing number of iteration (see, for example [9]). One approach to mitigate this effect involves incorporating prior knowledge about the the distribution of isotope activity through the use of regularization. In this context of ML estimation, such prior information can be integrated into the likelihood function to yield maximum a posteriori (MAP) estimate. Both MLEM and OSEM algorithm can be extended by introducing Gibbs prior distribution with smooth energy function. However in practical implementation, the prior can be evaluated only at the current estimate of the activity distribution. This leads to the MAP-EM one step late (OSL) in case of MLEM and it was introduced in [6]. In case of OSEM the same extension can be applied naturally, resulting in OSEM-OSL algorithm.

The non-smooth total variation (TV) functional is widely used in imaging applications for noise suppression. It promotes piecewise-constant solutions by allowing intra-region smoothing while preserving sharp edges at region boundaries, thereby avoiding over-smoothing effects common to traditional regularizers. However OSL method requires smooth energy function when incorporating a Gibbs prior. To address this, smoothed version of TV functional introduced to the OSL framework in [11, 12]. Despite their theoretical appeal, the use of smoothed TV and its derivative has been shown to include checker-board artifacts under strong regularization conditions in [16]. This is particularly problematic when strong regularization is required to achieve acceptable image quality, for e.g. when the signal-to-noise ration (SNR) of the SPECT scan is low.

To overcome these limitations, we propose a hybrid reconstruction scheme that integrates OSEM algorithm with Condat–Vu variant of the primal-dual hybrid gradient (PDHG) method, enabling the use of the original non-smooth version of the TV functional as a regularizer. The PDHG algorithm introduced in [3], is well suited for convex optimization problems involving linear maps

and non-smooth term, and its flexibility allows for direct incorporation of TV without the requirement of smoothing. The Condat–Vu algorithm presented in [4] and [18], extends PDHG by including an explicit gradient step for functions with Lipschitz-continuous derivatives. Both the original PDHG method and Condat–Vu algorithm can be enhanced through diagonal preconditioning, as proposed in [13], to further improve convergence behavior.

In our approach, the explicit gradient step, which is unique to the Condat–Vu extension of PDHG algorithm, is replaced by an OSEM update, which serves as an approximation of the MLEM update step, interpreted as a diagonally preconditioned gradient ascent on the log-likelihood. This hybrid method effectively suppresses noise while preserving fine structural details, and importantly, it eliminates checkerboard artifacts even under strong regularization. As a result, the proposed framework is particularly well suited for low-SNR SPECT imaging scenarios, where conventional smoothed-TV-based methods tend to fail.

2. Methods

2.1. SPECT projector operator

Our custom SPECT projector operator is based on the methods described in [17]. It performs rotation-based forward and backward projection on the GPU, incorporating distance-dependent modelling of both spatial resolution and detector sensitivity. Additionally, it is capable of material map based attention modelling. Attenuation coefficients are sourced from XCOM Photon cross section database provided by NIST at [1]. The current implementation does not include correction for radioactive decay. The projector was calibrated against the Teratomo™ Monte Carlo photons transport simulator developed by Mediso Ltd, which serves as the projection model for clinically validated multi pinhole (MPH) SPECT reconstruction. (See for e.g. in [8] and [2].) Although our implementation has been not directly calibrated using physical measurements, it has demonstrated compatibility with data acquired with AnyScan SPECT systems (Mediso Ltd, Hungary) equipped with parallel-hole collimators.

2.2. Penalized likelihood with Total Variation prior

We will consider the *linear Poisson measurement model*, which is commonly employed in SPECT reconstruction. The statistical model for the SPECT measurement is

$$b_i \sim \text{Poisson}\left\{(Au)_i + r_i\right\} \quad i = 1, \ldots, N,$$

where $b_i \geq 0$ denotes the number of photons counted in i-th bin of the measurement image, $u_j \geq 0$ represents the radionuclide activity at voxel $j = (x, y, z)$ and r_i denotes the expected contribution from random events, such as background radiation and scatter. The system matrix A models the detector geom-

etry and efficiency, attenuation and scan duration with non-negative elements $a_{i,j} \geq 0$.

The goal of reconstruction is to estimate the activity distribution u from the observed measurement data b, given the system matrix A and the estimated random events r. This is typically achieved by minimizing the *negative log-likelihood* of the Poisson model. Ignoring constant terms that do not depend on the variables to be minimized, the negative log-likelihood is given by

$$L(v) = \sum_{i=1}^{N} v_i - b_i \log v_i,$$

where $v = Au + r$ denotes the expected counts in the measurement domain.

As it was mentioned previously, iterative SPECT reconstruction methods are known to accumulate noise as the number of iteration increases. To mitigate this effect, prior information is typically incorporated into objective function in the form of a regularization term. Among various choices, the TV functional is frequently used in tomography reconstruction due to its favorable property of suppressing noise while preserving sharp edges between homogeneous regions. The discretized TV is defined as

$$\|\nabla u\|_{2,1} = \sum_{j} \left(\left(\delta_1^+ u\right)_j^2 + \left(\delta_2^+ u\right)_j^2 + \left(\delta_3^+ u\right)_j^2 \right)^{1/2}, \tag{2.1}$$

with $j = (x, y, z)$ denotes the voxel index and δ_d^+ is the forward finite difference operator along the d-th spatial direction with homogeneous Dirichlet boundary conditions (i.e. zero padding) and voxel spacing $h = (h_1, h_2, h_3)$.

At every point of the discretized scalar field u, the gradient ∇u indicates the direction of steepest ascent, the magnitude of the gradient representing the rate of change along that direction, so in essence $\|\nabla u\|_{2,1}$ is the sum of all rates of changes along the direction. Consequently $\|\nabla u\|_{2,1}$ can be interpreted as the aggregated magnitude of local variations in u. This quantity is strongly correlated with noise on the reconstructed image, making TV a natural choice for regularization in the SPECT reconstruction objective function.

The objective function for the SPECT reconstruction with TV prior can be formulated as

$$\tilde{L}(u) + R(\nabla u) + I(u), \tag{2.2}$$

where $\tilde{L}(u) = L(Au + r)$ represents the data fidelity term based on the negative log-likelihood, $R(\nabla u) = \beta \|\nabla u\|_{2,1}$ is the regularization term weighted by the regularization parameter $\beta > 0$ and $I(u)$ is the convex indicator function enforcing non-negativity of the solution:

$$I(u) = \begin{cases} 0, & \text{if } u \geq 0 \\ +\infty & \text{otherwise.} \end{cases}$$

This formulation defines a convex, non-smooth optimization problem.

2.3. Non-smooth TV regularized SPECT reconstruction

2.3.1. Finding an ML solution

The classical MLEM [15] based SPECT reconstruction method can be used to obtain a ML estimate of u by minimizing the function $\tilde{L}(u) = L(Au + r)$. Starting from an initial estimate $u^{(0)}$ with $u_j^{(0)} \geq 0$ the activity at voxel j updated iteratively according to the following multiplicative update rule:

$$u_j^{(k+1)} = \frac{u_j^{(k)}}{\sum_i a_{i,j}} \sum_i a_{i,j} \frac{b_i}{\sum_s a_{i,s} u_s^{(k)} + r_i}. \tag{2.3}$$

The multiplicative update in Equation (2.3) can be interpreted as diagonally preconditioned gradient descent step on the objective function, as described in [10]:

$$u^{(k+1)} = u^{(k)} - T\left(u^{(k)}\right) A^T L'(Au^{(k)} + r), \tag{2.4}$$

where the diagonal preconditioning matrix is $T(u) = D(u)D\left(A^T\mathbf{1}\right)^{-1}$ with $D(x)$ denoting the the diagonal matrix formed from the vector x, and $\mathbf{1}$ is the vector of all ones.

A known limitation of MLEM is its slow convergence rate. The primary computation burden arises from the evaluation of the forward- and backward-projection operators A and A^T during each iteration. To address this issue, the OSEM algorithm was introduced in [7]. OSEM accelerates the convergence by updating the estimate u using only a subset of the measurement data at each iteration. Specifically, the measurement indices $\{1, \ldots, N\}$ are partitioned into M (typically disjoints) subsets $S_m \subset \{1, \ldots, N\}$ for $m = 0, \ldots, M-1$. Then the MLEM update rule from Equation (2.3) is modified as follows:

$$u_j^{(k+1)} = \frac{u_j^{(k)}}{\sum_{i \in S_m} a_{i,j}} \sum_{i \in S_m} a_{i,j} \frac{b_i}{\sum_s a_{i,s} u_s^{(k)} + r_i}, \tag{2.5}$$

where $m = k \bmod M$.

The negative log-likelihood can be decomposed over the subsets as $L(v) = \sum_m L_m(v_m)$ with

$$L_m(v_m) = \sum_{i \in S_m} v_i - b_i \log v_i$$

where v_m is the restriction of the vector v to the indices in S_m. The OSEM update in Equation (2.5) can also be interpreted as diagonally preconditioned gradient descent step:

$$u^{(k+1)} = u^{(k)} - T_m\left(u^{(k)}\right) A_m^T L_m'(A_m u^{(k)} + r_m), \tag{2.6}$$

with the diagonal preconditioning matrix $T_m(u)$ defined as:

$$T_m(u) = D(u)D\left(A_m^T\mathbf{1}\right)^{-1} \tag{2.7}$$

where A_m is the submatrix of A containing the rows indexed by S_m and r_m is the corresponding subvector of r. While MLEM converges to a ML solution under mild assumptions, OSEM may instead cycle among at most M limit points, which typically lie close to the ML estimate.

2.3.2. Primal-dual TV regularization

Let us denote the *convex conjugate* of a proper, convex function f with f^* defined as $f^*(y) = \sup_x \langle y, x\rangle - f(x)$, where $\langle\cdot,\cdot\rangle$ denotes the standard inner product.

The regularization function R is closed and convex and there exists a feasible $u > 0$ such that $\tilde{L}(u) + R(\nabla u) < \infty$. Therefore, the conditions of Fenchel's Duality Theorem (see Section 31 in [14]) are satisfied, and strong duality holds between the *primal problem*, in which we try to minimize objective function defined in Equation (2.2) and its *dual problem* which seeks to maximize the following dual objective: $-R^*(g) - (\tilde{L} + I)^*(\nabla^* g)$. The adjoint of discrete gradient operator, ∇^* is the negative of the discrete divergence operator, defined as $(\mathrm{div} g)_j = \left(\delta_1^- g_1\right)_j + \left(\delta_2^- g_2\right)_j + \left(\delta_3^- g_3\right)_j$, where δ_d^- denotes the backward finite difference operator along direction d. In this formulation, the variable u in the primal objective function in Equation (2.2) is referred to as the *primal variable*, while the variable g in the dual objective, is known as the *dual variable*.

If u minimizes the primal objective of Equation (2.2) and g maximizes the dual objective, then the pair (u, g) constitutes a saddle point of the associated Lagrangian defined as

$$(u, g) \mapsto \langle \nabla u, g\rangle - R^*(g) + \tilde{L}(u) + I(u). \tag{2.8}$$

This saddle point formulation provides the foundation for primal-dual optimization methods such as the PDHG algorithm.

The *proximal mapping* of f at point x, with a symmetric positive definite step-size matrix S, is defined as

$$\mathrm{prox}_f^S(x) = \arg\min_z \left(f(z) + \frac{1}{2}\|z - x\|_S^2 \right),$$

where $\|x\|_S = \sqrt{\langle S^{-1}x, x\rangle}$ is the norm induced by S. If f is differentiable, the proximal mapping reduces to $\mathrm{prox}_f^S(x) = x - Sf'(x)$, which can be interpreted as a preconditioned implicit gradient descent step.

The Condat–Vu extension of PDHG algorithm, introduced in [4], is designed to search for saddle point of the Lagrangian defined in Equation (2.8). Let us assume that the step-size matrices S and T are diagonal with positive entries. At each iteration, the method updates the dual variable g according to the rule:

$$g^{(k+1)} = \mathrm{prox}_{R^*}^S\left(g^{(k)} + S\nabla u^{(k)}\right).$$

The convex conjugate R^* is the convex indicator function of ℓ_∞-norm ball of radius β. Therefore, the proximal mapping $\text{prox}^S_{R^*}$ reduces to a projection onto this convex set. Since S is diagonal, the projection simplifies to the final version of the dual step:

$$\text{prox}^S_{R^*}(g) = \frac{g}{\max\left(1, \frac{\|g\|_2}{\beta}\right)}.$$

After each dual variable update, the primal variable u is updated according to the following rule:

$$u^{(k+1)} = \text{prox}^T_I\left(\overline{u}^{(k+1)} + T\text{div}\left(2g^{(k+1)} - g^{(k)}\right)\right), \tag{2.9}$$

where $\overline{u}^{(k+1)} = u^{(k)} - TA^TL'(Au^{(k)} + r)$ is the diagonally preconditioned explicit gradient step with respect to the negative log-likelihood. The term $\text{div}\left(2g^{(k+1)} - g^{(k)}\right)$ is an extrapolated dual variable used to improve convergence.

The proximal mapping of I corresponds to the projection onto the feasible set defined by the convex indicator function I, which in this case is the non-negative orthant. Therefore, the update simplifies to $\text{prox}^T_I(u) = \max(u, 0)$

The convergence of the algorithm is guaranteed under the condition that the following induced matrix norm satisfies

$$\left\| S^{1/2}\nabla\left(T^{-1} - \frac{\mu}{2}I\right)^{-1/2}\right\|^2 < 1, \tag{2.10}$$

where μ is a Lipschitz constant of the gradient of the data fidelity term $\tilde{L}$. Under this condition, the algorithm converges to saddle point $(\hat{u}, \hat{g})$, where $\hat{u}$ is the solution of the primal problem defined in Equation (2.2), regardless of the initial point $(u^{(0)}, g^{(0)})$. If $r > 0$, then $\tilde{L}$ has Lipschitz-continuous gradient. In context of SPECT imaging, the present of background radiation is inevitable, making the assumption realistic and well justified.

2.3.3. Primal-dual TV regularized OSEM reconstruction

Our proposed method combines the Condat–Vu algorithm with OSEM. The term $\overline{u}^{(k)} = u^{(k)} - TA^TL'(Au^{(k)} + r)$ which appears in the primal variable update defined in Equation (2.9), can be interpreted as a preconditioned gradient descent step on $\tilde{L}(u)$. By choosing the preconditioning matrix as $T = D\left(u^{(k)}\right) D\left(A^T\mathbf{1}\right)^{-1}$, this expression corresponds to the additive form MLEM update defined in Equation (2.4).

To accelerate the computation, we adopt the subset-based strategy of OSEM algorithm. Specifically we replace the full system matrix A with a subset A_m, where $m = k \bmod M$ and use the corresponding preconditioning matrix $T_k = D\left(u^{(k)}\right) D\left(A_m^T\mathbf{1}\right)^{-1}$. With this modification, the update $\overline{u}^{(k)}$ can be computed via the multiplicative OSEM update step in Equation (2.5).

In our framework, the primal step-size matrix T_k changes at every iteration due to its dependence on the current estimate $u^{(k)}$. Consequently, the dual step size matrix S_k must also adapt accordingly. The Lipschitz-constant μ might not be available in every case. Instead of enforcing condition which requires the value μ defined in Equation (2.10), we adopt a simplified criterion based on the original PDHG formulation for matrix-valued step sizes described in [13]. Specifically, at each iteration, we require:

$$\left\| S_k^{1/2} \nabla T_k^{1/2} \right\|^2 < 1. \tag{2.11}$$

If the dual variable step-size is the scalar

$$S_k = \frac{\rho}{\|T_k\| \, \|\nabla\|^2},$$

then

$$\begin{aligned} \left\| S_k^{1/2} \nabla T_k^{1/2} \right\|^2 &\leq S_k \, \|\nabla\|^2 \left\| T_k^{1/2} \right\|^2 = \\ &= S_k \, \|\nabla\|^2 \, \|T_k\| = \\ &= \frac{\rho}{\|\nabla\|^2 \, \|T_k\|} \, \|\nabla\|^2 \, \|T_k\| = \\ &= \rho. \end{aligned}$$

Therefore, if $0 < \rho < 1$, then S_k and T_k satisfy Equation (2.11). In practice, ρ is chosen close to 1; in our experiments, we used $\rho = 1 - 10^{-3}$. Since T_k is a diagonal matrix, its norm $\|T_k\|$ reduces to the maximum diagonal entry. The operator norm $\|\nabla\|$ of the discrete gradient operator can be efficiently estimated by power iteration.

The regularization step might lead to non-positive entries in the updated primal variable $u^{(k+1)}$, and the negative entries are projected to zero by the proximal operator of the non-negativity constraint I. Where the activity values are exactly zero, the multiplicative nature of OSEM updates prevents further modifications of those voxels. To enure strict positivity and maintain the availability of updates, the indicator function $I(u)$ can be replaced by a relaxed constraint $I_c(u)$ which is the convex indicator function of the set $\{u \geq c\}$ where $c > 0$ is a small constant. The corresponding proximal mapping becomes a simple thresholding function $\text{prox}_{I_c}^T(u) = \max(u, c)$.

2.3.4. Compensation of the dependence on system-sensitivity in regularization strength

When attenuation is included in the system matrix A, the *system-sensitivities* $A_m^T \mathbf{1}$ associated with subset $m = k \bmod M$ become spatially inhomogeneous. As a result, the regularization update term in the primal variable update in Equation (2.9) can lead spatially varying regularization strength (see Section 3.1). This effect is also noticeable in case of OSL. (See for e.g. [20].)

To compensate this effect, we can scale subgradient term by diagonal matrix formed from the system sensitivities, $D\left(A_m^T\mathbf{1}\right)$, effectively canceling the inverse scaling from the step size matrix. The same modification was proposed to OSL based methods in [16, 20]. This yields the sensitivity-compensated update:

$$u^{(k+1)} = \operatorname{prox}_I^{T_k}\left(\overline{u}^{(k+1)} + D\left(u^{(k)}\right)\operatorname{div}\left(2g^{(k+1)} - g^{(k)}\right)\right). \tag{2.12}$$

This adjustment restores regularization homogeneity across the image, ensuring consistent noise suppression regardless of sensitivity variations introduced by attenuation modelling.

2.4. OSEM-PDHG-TV method

The computational requirements of the proposed algorithm are comparable to those of the OSEM-OSL method equipped with a smoothed version of the TV prior. However, the proposed method requires additional memory to store the dual variable (i.e., the gradient field). Furthermore, to implement over-relaxation, the dual variable must be stored twice. For SPECT imaging with a resolution of 256 voxels in each dimension and 32-bit floating-point storage, this results in an additional memory usage of approximately 128 MB. The algorithm is presented in Algorithm 1.

Algorithm 1 OSEM-PDHG-TV

procedure OSEM-PDHG-TV
  $u, g \leftarrow c\mathbf{1}, 0$
  for $l = 1, \ldots, L$ **do**
    for $m = 1, \ldots, M$ **do**
      $S \leftarrow \frac{\rho\left\|A_m^T\mathbf{1}\right\|_\infty}{\|\nabla\|^2\cdot\|u\|_\infty}$
      $g' \leftarrow \frac{g+S\nabla u}{\max\left(1, \frac{\|g+S\nabla u\|_2}{\beta}\right)}$ ▷ Dual variable update
      $u_j \leftarrow \frac{u_j}{\sum_{i\in S_m} a_{i,j}} \sum_{i\in S_m} a_{i,j} \frac{b_i}{\sum_s a_{i,s}u_s + r_i}$ ▷ OSEM update for all j
      $u, g \leftarrow u + D(u)\operatorname{div}\left(2g' - g\right), g'$
      $u \leftarrow \max\left(u, c\right)$
    end for
  end for
  return x
end procedure

2.5. Phantom simulations

To evaluate the performance of the proposed hybrid OSEM-PDHG-based reconstruction method, we conducted a series of simulations using a digital Deluxe Jaszczak phantom. The simulations were performed with the Monte Carlo photon transport simulator developed by Mediso Ltd.

The imaging setup replicated a clinical acquisition scenario using a Mediso AnyScan TRIO SPECT system equipped with LEHR-HS collimator with NaI crystal of 9.5mm thickness. The phantom was filled with 600MBq ^{99m}Tc activity and it included several distinct regions:

1. a homogeneous region filled with uniform activity and no inserts, used for noise assessment;
2. six non-radioactive cold spheres embedded in hot background, with diameters of 9.5mm, 12.7mm, 15.9mm, 19.1mm, 25.4mm, and 31.8mm;
3. six segments containing non-radioactive rods within hot background. The rods have diameter of 4.8mm, 6.4mm, 7.9mm, 9.5mm, 11.1mm, and 12.7mm.

The last two regions are visualized in Figure 1, highlighting the cold inserts in the hot background.

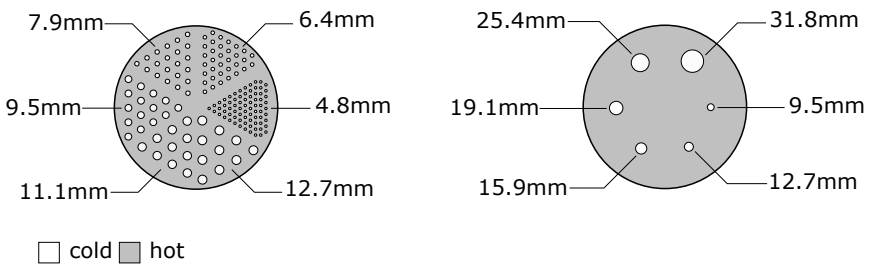

Figure 1. Cold inserts of the Deluxe Jaszczak phantom.

During the simulated acquisition, a single SPECT head operated in step-and-shoot mode, capturing measurements of the phantom from 120 angular positions with 3° increments between views. Two energy windows were used to record detected photons: a 20% main window around 140 keV, and an adjacent 7% lower-energy scatter window, intended for scatter correction.

Detected photon events were binned into frames of 256×256 pixels. The Monte Carlo simulator was configured to account for various physical interactions, including photon scattering in phantom, collimator, crystal and in the back-compartment of the SPECT head Additionally photon rejection due to camera's energy resolution was modelled using Gaussian distribution.

To evaluate reconstruction performance under varying noise conditions, we generated three distinct datasets, each consisting of 10 independent measurement realization:

- medium SNR simulated acquisitions denoted by M_{120}, where each scan contains approximately 120 million detected event, corresponding to a frame acquisition time of ∼40s;

- low SNR scans, denoted by M_{30} containing approximately 30 million events per measurement, with a frame duration of ∼10s;
- very low SNR set, denoted by M_{15}, including approximately 30 million, with a frame duration of ∼5s.

For each measurement realization, the total number of photon hits was sampled from a Poisson distribution with an expected value of 15, 30, or 120 million counts, depending on the dataset. Given the sampled total count, individual pixel values in the measurement image were then drawn from a multinomial distribution, conditioned on the mean values of the Poisson variables produced by the simulator.

2.6. Performance indicators

To quantitatively assess reconstruction performance, we used several standard performance metrics.

Peak signal-to-noise ratio (PSRN) measures the fidelity of the reconstructed image u relative to a known ground truth u^*. It is defined as:

$$\mathrm{PSNR}\,(u, u^*) = 20 \log_{10} \left(\frac{\mathrm{MAX}\,(u^*)}{\mathrm{RMSE}\,(u, u^*)} \right),$$

where $\mathrm{MAX}\,(u^*)$ is maximum value of the reference image u^* and RMSE denotes the root mean square error calculated as:

$$\mathrm{RMSE}\,(u, u^*) = \sqrt{\frac{1}{n} \sum_j \left(u_j - u_j^*\right)^2},$$

where n is the number of voxels.

Structural similarity index measure (SSIM), introduced in [19], is a perceptual metric used to evaluate the similarity between two images by modeling human visual perception. SSIM compares local patterns of pixel intensities that have been normalized for luminance and contrast, making it more sensitive to structural information. The values ranges from -1 to 1, where 1 indicates perfect similarity between images.

The noise level (NL) is used to characterize the measured noise in a specific volume of interest (VOI). It is defined as the coefficient of variation within the VOI:

$$\mathrm{NL}_{\mathrm{VOI}} = \frac{\sigma_{\mathrm{VOI}}}{\mu_{\mathrm{VOI}}},$$

where σ and μ are the the standard deviation and mean, respectively.

Contrast-to-noise ratio (CNR) is employed to evaluate the contrast between cold regions and the surrounding hot background in the phantom. It is computed as:

$$\mathrm{CNR}_{\mathrm{VOI}} = \frac{\mu_{\mathrm{BG}} - \mu_{\mathrm{VOI}}}{\mu_{\mathrm{BG}}},$$

where BG stands for background VOI.

2.7. Reference method

To benchmark the performance of the proposed method, we compare it against an equalized OSEM-OSL method as it was described in [16]. While this method was created for PET reconstruction, it can be applied to SPECT reconstruction as well, as demonstrated in [20].

In contrast to the traditional OSL method presented in [6], this method includes system-sensitivity compensation of the regularization term. The update rule for the reference method is given by:

$$u_j^{(k+1)} = \frac{1}{1+\beta\partial_j V(u^{(k)})} \cdot \frac{u_j^{(k)}}{\sum_{i\in S_m} a_{i,j}} \sum_{i\in S_m} a_{i,j} \frac{b_i}{\sum_s a_{i,s} u_s^{(k)} + r_i},$$

where $\beta > 0$ controls the regularization strength and $\partial_j V(u)$ denotes the partial derivatives of the smoothed TV functional with respect to voxel j. The regularization functional is defined as:

$$V(u) = \sum_j \left(\left(\delta_1^+ u\right)_j^2 + \left(\delta_2^+ u\right)_j^2 + \left(\delta_3^+ u\right)_j^2 + \eta^2 \right)^{1/2}, \tag{2.13}$$

where $\eta > 0$ is a small smoothing parameter, introduced in [12].

3. Results

3.1. Regularization homogeneity

When the Jaszczak phantom is positioned in the center of the FOV, the effective strength of regularization can vary radially from the axis of rotation of the SPECT heads–if no compensation is applied. To quantify this effect, three different cylindrical VOIs are placed symmetrically within the homogeneous region, positioned at increasing radial distance on either side of the phantom center. These VOIs are used to measure the NL, which serves as a proxy for regularization strength. Higher NL indicates weaker regularization. By averaging the NL values from mirrored VOIs across the rotation axis, we obtain a robust indicator of radial regularization inhomogeneity.

We evaluated the impact of regularization strength inhomogeneity caused by the system-sensitivity dependence of the step-size, by running the OSEM-PDHG algorithm with TV prior on one measurement from the M_{120} group without compensation, i.e. the primal update step was Equation (2.9). To demonstrate that the system-sensitivity compensated version of the proposed method is not suspectable to this phenomenon, we also performed reconstruction on the same measurement with primal variable update rule of Equation (2.12).

The number of subsets was set to 12, and the reconstruction was performed for 100 iterations, resulting in a total of 1200 volume updates. To ensure fair comparison, the regularization strength β in both cases was chosen in such way

that the NL in the inner region of the phantom was close to equal. For the non-compensated version, $\beta = 10^{-5}$ and for the compensated version, a higher value of $\beta = 1.5 \cdot 10^{-3}$ was used to compensate the canceled system sensitivities of the solution.

For both reconstruction variants, the NL values in the **inner**, **middle** and **outer** VOIs were recorded at iterations 25, 50, 75 and 100. The results are presented in Figure 2. In the non-compensated reconstruction, a clear radial inhomogeneity is observed: NL values differ significantly between regions, and this discrepancy increases as the number of iterations grows. In contrast, the compensated version maintains consistent regularization, with slight differences across the regions.

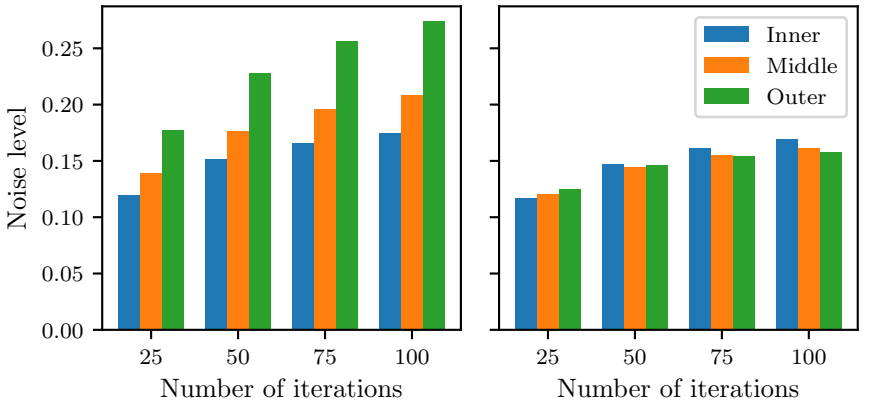

Figure 2. NL measured radially placed VOIs across reconstruction iterations. In the **non-compensated** version (left), NL varies significantly across regions, with discrepancy increasing as the number of iterations grow. In contrast, the **compensated** case shown only minor differences in NL between regions, indicating improved regularization homogeneity.

These results demonstrate that enabling compensation for system-sensitivity in the step-size matrix during regularization update leads to more homogeneous regularization across the image volume. Compared to the non-compensated approach, the choice of regularization parameter β becomes more straightforward and less sensitive to spatial variations. This has practical significance in clinical settings, as it simplifies the calibration of reconstruction protocols, thus allowing effective fine-tuning using simpler phantoms rather than complex or anatomical realistic models.

3.2. Maximum regularization strength

To evaluate the maximum effective regularization strength of the OSL and PDHG based reconstruction methods, we performed a series of reconstruction on one of the measurements from the M_{120} dataset using 12 subsets and 10 iterations. The regularization parameter β was varied across runs, with values

defined as $\beta = (k+1) \cdot 10^{-3}$ for $k = 0, \ldots, 11$. Following each reconstruction, the NL was measured in the homogeneous region of the phantom to quantify the extent of regularization. The results are presented in Figure 3, illustrating how NL varies with increasing values of β for both reconstruction methods. Notably, up to a certain threshold, both methods exhibit similar regularization strength for the same β values, indicating consistent behavior in low-to moderate regularization regime.

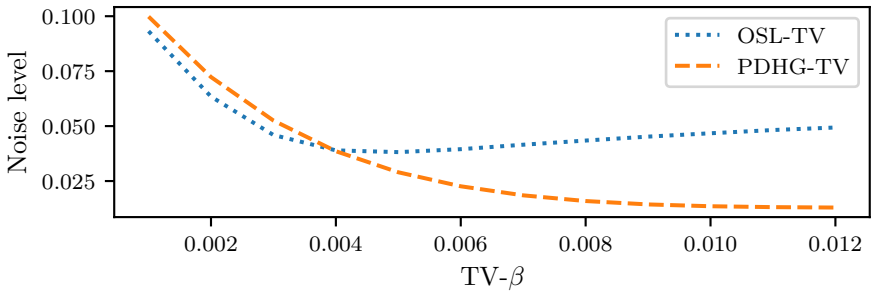

Figure 3. *Maximum achievable regularization strength for OSL and PDHG based methods.* For **OSL**, the lowest NL is observed around $\beta = 4{\cdot}10^{-3}$. Beyond this point the checker-board artifacts become increasingly prominent, leading to degradation in NL, despite stronger regularization. In contrast **PDHG** is not affected by checker-board artifact. It reaches minimum NL at $\beta = 10^{-2}$, after which further increases in β do not yield additional noise reduction.

In the OSL method, the potential function of the Gibbs prior needs to be evaluated at every iteration. This potential corresponds to the the gradient of the smoothed version of TV function defined in Equation (2.13). However, computation of the partial derivatives of the smoothed TV introduces checker-board pattern observed in reconstruction. This phenomenon previously was reported in [16], and is clearly visible in our results, as illustrated in Figure 4.

3.3. Reconstruction performance

All reconstruction were performed using 10 iterations with 12 subsets, resulting in total of 120 volume updates per reconstruction. For each simulated scan in the three datasets (M_{120}, M_{30} and M_{15}), we identified the regularization parameter β_0 that yielded the highest average PSRN across the dataset when using equalized OSL reconstruction with smoothed TV regularization. As discussed in Section 3.2, the regularization parameter β is comparable between OSL and PDHG methods. Therefore we have used the same β_0 values as reference points for PDHG based reconstruction with non-smooth TV prior. In addition to β_0, we also evaluated performance of PDHG based method at two increased regularization levels, β_1 and β_2. The specific values of β_0, β_1 and β_2 used in each dataset are summarized in Table 1.

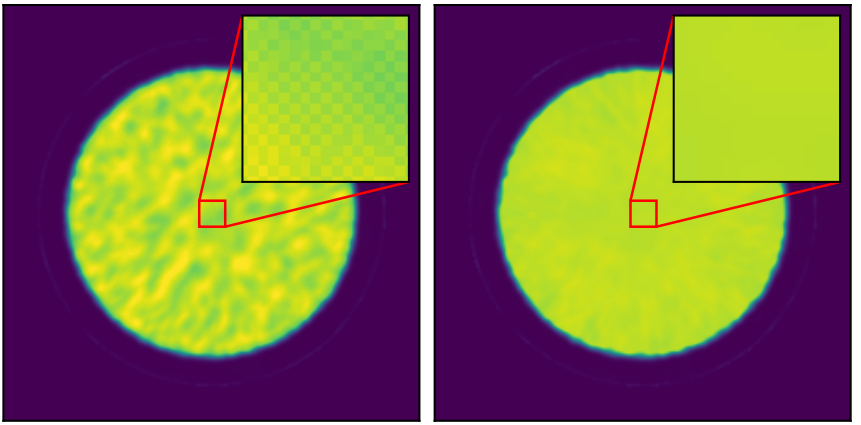

Figure 4. *Checker-board artifacts in TV-regularized OSL reconstruction.* **Left:** OSL based regularization exhibits prominent checkerboard artifacts due to the use of smoothed TV regularization. **Right:** PDHG based regularization, no visible artifacts. Both reconstruction were performed with $\beta = 1.2 \cdot 10^{-2}$. The NL values in this region can be seen in Figure 3 for both reconstruction methods.

Dataset	β_0	β_1	β_2
M_{120}	$3.5 \cdot 10^{-3}$	$4 \cdot 10^{-3}$	$4.5 \cdot 10^{-3}$
M_{30}	$8 \cdot 10^{-3}$	$9 \cdot 10^{-3}$	10^{-2}
M_{15}	$1.2 \cdot 10^{-2}$	$1.3 \cdot 10^{-2}$	$1.4 \cdot 10^{-2}$

Table 1. Regularization strength parameters β_0, β_1 and β_2 used for the PDHG-based TV reconstruction. The value β_0 corresponds to the regularization strength at which the OSL method with smoothed TV achieves the maximum mean PSNR, and serves as a reference for comparison.

We evaluated the reconstruction results using several quantitative metrics: PSRN, SSIM, NL, and the CNR of both the cold rods and cold spheres. Statistical comparison was performed using Welch's t-test to asses wether the difference in means is significant relative to the reference method. The analysis revealed no statistically significant differences in the cold sphere contrast across any of the reconstruction settings when compared to the the reference. The minimum observed p-value was 0.3304. As a result, the cold sphere CNRs were excluded from further analysis and are not shown in the figure. The mean relative performance indicators, along with the absolute mean values, are presented in Figure 5.

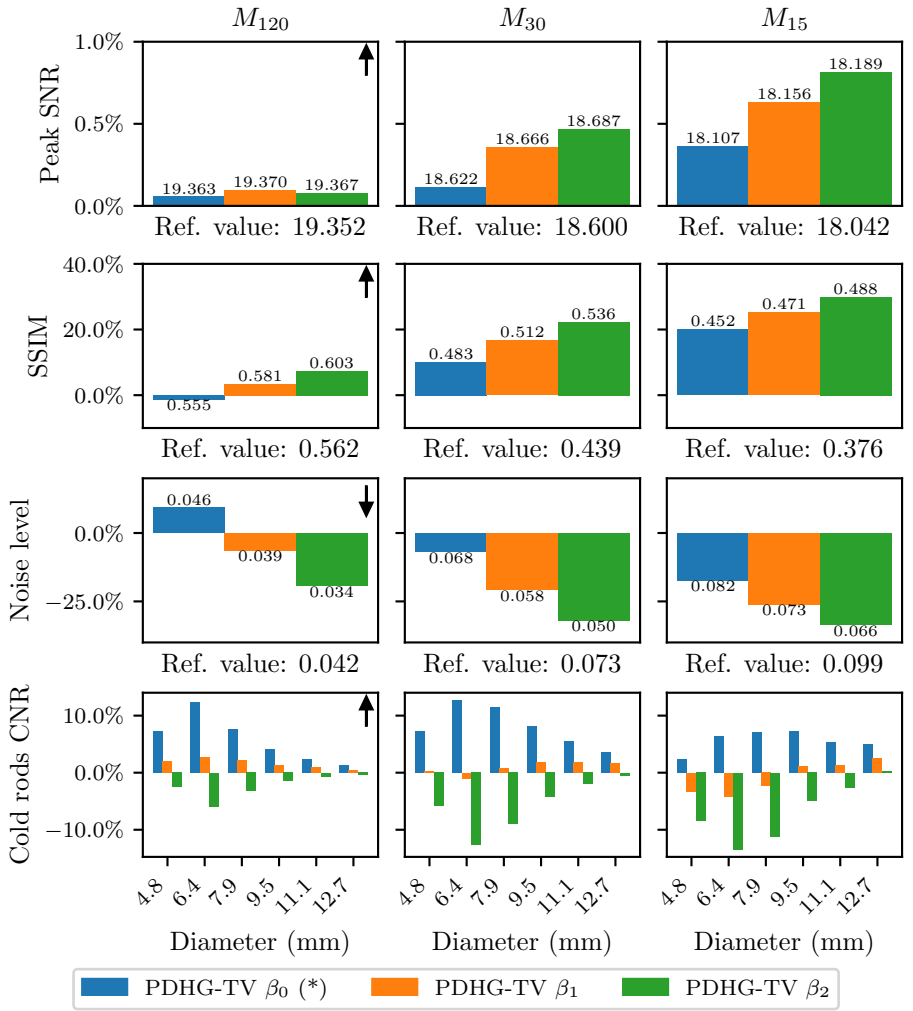

Figure 5. *Relative performance indicators compared to OSL-TV method with regularization parameter* β_0. Arrows indicate the direction of improvement for each metric. Absolute values of the indicators are displayed above each bars, while the corresponding reference values are shown below the plots. Asterisks (*) denote the reconstruction that used the same regularization strength parameter (β_0) as the reference.

Across all datasets, the mean PSRN improves when using the same regularization strength parameter β_0 used in PDHG based TV reconstruction compared to the OSL-TV reference. The relative improvement in PSRN becomes more pronounced as the total counts of the measurement decreases. When regularization strength is increased to β_1, PSRN improves further for all datasets,

with the most significant gains observed in the lowest-SNR dataset. Upon increasing the regularization strength to β_2, a decrease in PSRN observed for M_{120} compared to β_1, although the metric continues to improve for M_{30} and M_{15}.

In term of SSIM, all datasets but M_{120} show an increase when using β_0 in PDHG-TV. As with PSRN, the relative improvement in SSIM increases with decreasing measurement total counts. Further increases in the regularization strength to β_1 β_2 lead additional SSIM gains in all datasets, again with larger improvements in the lower-SNR conditions.

A similar trend is observed in the NL measured in the homogeneous region of the phantom. For the M_{120} dataset using β_0 results in a slight increase in NL compared to the OSL reference. However, for both M_{30} and M_{15}, the NL is lower than that of the reference, with relative improvement increasing as measurement SNR decreases. Increasing regularization strength further (to β_1 and β_2), leads to additional reduction in NL across all datasets; the decrease is greater when SNR of the measurement is lower. A strong correlation is observed between SSIM and NL: lower noise levels in the homogeneous regions are associated with higher SSIM values.

Regarding the CNR of the cold rods, PDHG-TV consistently outperforms OSL-TV when using the same regularization parameter β_0. For the M_{120}, the improvement is more noticeable in sectors containing rods below the spatial resolution limit of the reconstruction (i.e. rods that are not visible resolved). Thus, these improvements can be ignored from the analysis. In lower-SNR datasets M_{30} and M_{15}, contrast improvements are also observed in the sectors where rods are visible. However, increasing the regularization strength to β_1 reduces the contrast to levels comparable to OSL-TV reference. Further increasing to to β_2 leads to additional drop in CNR across all datasets in each rod sectors, primarily due to the blurring effect of stronger regularization.

In summary, all performance indicators, except for the contrast of cold rods, benefit from increased regularization strength in the PDHG-TV method. These improvements are more substantial in lower-SNR conditions. However this gain comes at the cost of reduced CNR for cold rods, highlighting a tradeoff between noise suppression and contrast preservation.

Representative reconstruction results from the M_{15} dataset are shown in Figure 6. Qualitatively, the PDHG-TV method using the reference regularization parameter β_0 exhibits noticeably lower NLs, visible in the homogeneous background of a slice containing the cold spheres. Additionally, reduced blurring in the cold rod region results in higher visual contrast at β_0. However this advantage diminishes as the regularization strength increases to β_1 and β_2, where blurring effect is more pronounced and leads to loss in rod contrast. The contrast of the spheres appears visually consistent across all reconstructions, aligning with the quantitative findings.

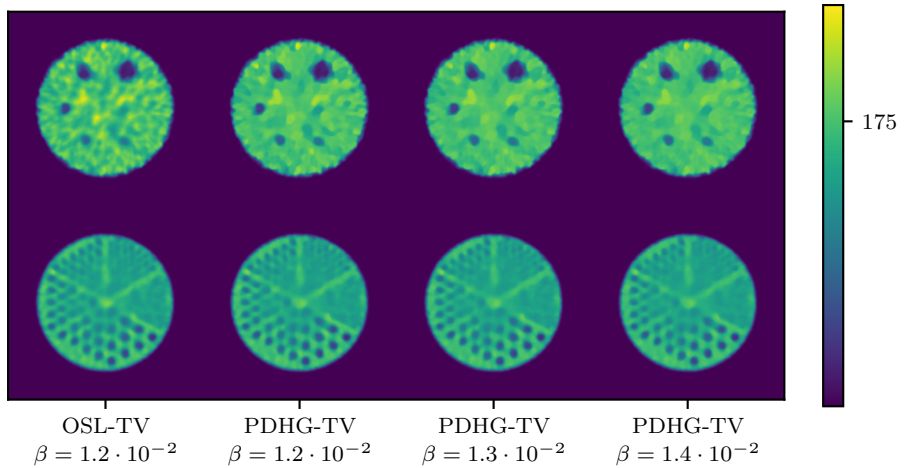

Figure 6. *Reconstructed slice showing cold spheres and cold rods from a M_{15} measurement across different regularization strengths.* The voxel intensity 175 Bq corresponds to the hot region in the simulated phantom. **First:** Reference reconstruction using OSL-TV. **Second:** PDHG-TV with the same regularization parameter β_0. This reconstruction shows reduced NL in the cold sphere slice and less blurring in the cold rods slice, resulting improved visual contrast. **Third and fourth:** Reconstruction with increased regularization parameter β_1 and β_2, which further reduce noise but also lead to greater blurring and reduced cold rod contrast.

4. Discussion

This work presents a hybrid image reconstruction framework that combines the well-established OSEM method with Condat–Vu algorithm to enable the use of non-smooth TV regularization in SPECT imaging. Since OSEM is already widely deployed in commercial SPECT systems, one of the strengths of this approach lies in the fact that the proposed extension of OSEM can be readily integrated into current reconstruction software with minimal disruption.

One of the central challenges in iterative reconstruction is tuning the regularization strength to balance noise suppression and detail preservation. Traditional OSL based regularization suffers from system-sensitivity dependence in regularization strength, which makes it hard to tune the regularization strength parameter β. As shown in Section 3.1, the formulation of hybrid OSEM-PDHG yielded by the theory also suffers from the effect. We addressed this by introducing a system-sensitivity compensation strategy that ensures spatially homogeneous regularization, even when attenuation is modelled. Our results show that this compensation improves consistency across the field of view and simplifies the task of selecting the regularization parameter β, particularly in clinical settings where robust protocol design is essential.

The proposed method also resolves an issue in OSL-based TV regularization: the emergence of checkerboard artifacts when using smoothed approximations of the TV functional. These artifacts limit the usable range of β in traditional methods, capping the achievable noise suppression as shown in Section 3.2. In contrast, our approach supports direct use of the non-smooth TV functional, allowing significantly higher regularization strengths without visual artifacts. This translates into improved noise reduction, especially in low-SNR scenarios such as short-duration scans or low-activity studies.

Our quantitative evaluation across simulated datasets with varying SNR levels confirmed these advantages. When using the same regularization strength parameter β_0, our approach outperformed OSL-TV in terms of PSRN, SSIM, and NL. The gains were more pronounced as the total counts of the measurement decreased. Moreover, unlike OSL-TV, the proposed method continued to improve as β increased, until eventually reaching a point of diminishing returns. This robustness enables greater flexibility in adjusting regularization strength for noise control.

Finally, the generality of the PDHG framework provides a foundation for future extension. In place of TV, other non-smooth regularizers, such as higher-order TV, directional priors, or learned convex penalties, can be integrated into the same reconstruction scheme. This extensibility makes the method a flexible platform for incorporating emerging advances in regularization design.

In summary, the proposed hybrid OSEM-PDHG framework offers a practical, high-performance solution for SPECT reconstruction that is both backward-compatible with clinical systems and forward-compatible with advanced regularization techniques. It improves reconstruction quality across varying noise levels, avoids common artifacts, and simplifies parameter tuning, making it an appealing tool for both clinical deployment and further research.

References

[1] **Berger, M.J. et al.,** XCOM-Photon Cross Sections Database, *NIST Standard Reference Database 8*, (2009). https://dx.doi.org/10.18434/T48G6X

[2] **Buchert, R. et al.**, Dopamine transporter SPECT with 12-minute scan duration using multiple-pinhole collimators, *Journal of Nuclear Medicine*, **65** (2024) 446–452. https://doi.org/10.2967/jnumed.123.266276

[3] **Chambolle, A. and Th. Pock,** A first-order primal-dual algorithm for convex problems with applications to imaging, *Journal of Mathematical Imaging and Vision*, **40** (2011) 120–145. https://doi.org/10.1007/s10851-010-0251-1

[4] **Condat, L.,** A primal-dual splitting method for convex optimization involving Lipschitzian, proximable and linear composite terms, *Journal of Optimization Theory and Applications*, **158** (2013) 460–479.
https://doi.org/10.1007/s10957-012-0245-9

[5] **Dempster, A.P., N.M. Laird, and D.B. Rubin,** Maximum likelihood from incomplete data via the EM algorithm, *Journal of the Royal Statistical Society. Series B* (*Methodological*), **39** (1977) 1–38.
https://www.jstor.org/stable/2984875
https://doi.org/10.1111/j.2517-6161.1977.tb01600.x

[6] **Green, P.J.,** Bayesian reconstructions from emission tomography data using a modified EM algorithm, *IEEE Transactions on Medical Imaging*, **9** (1990) 84–93.
https://doi.org/10.1109/42.52985

[7] **Hudson, H.M. and R.S. Larkin,** Accelerated image reconstruction using ordered subsets of projection data, *IEEE Transactions on Medical Imaging*, **13** (1994) 601–609.
https://doi.org/10.1109/42.363108

[8] **Krizsan, A.K. et al.,** Performance evaluation of a novel multi-pinhole collimator on triple-NaI-detector SPECT/CT for dedicated myocardial imaging, *EJNMMI Physics* **10** (2023) 24.
https://doi.org/10.1186/s40658-023-00541-y

[9] **Lalush, D.S. and B.M.W. Tsui,** Simulation evaluation of Gibbs prior distributions for use in maximum a posteriori SPECT reconstructions, *IEEE Transactions on Medical Imaging*, **11** (1992) 267–275.
https://doi.org/10.1109/42.141651

[10] **Lange, K. and R. Carson,** EM reconstruction algorithms for emission and transmission tomography, *Journal of Computer Assisted Tomography*, **8** (1984) 306–316.
https://pubmed.ncbi.nlm.nih.gov/6608535/

[11] **Panin, V.Y., G.L. Zeng, and G.T. Gullberg,** Total variation regulated EM algorithm [SPECT reconstruction]. *IEEE Transactions on Nuclear Science*, **46** (1999) 2202–2210.
https://doi.org/10.1109/23.819305

[12] **Persson, M., D. Bone, and H. Elmqvist,** Three-dimensional total variation norm for SPECT reconstruction. *Nuclear Instruments and Methods in Physics Research Section A: Accelerators, Spectrometers, Detectors and Associated Equipment*, **471** (2001) 98–102.
https://doi.org/10.1016/S0168-9002(01)00962-7

[13] **Pock, Th., and A. Chambolle,** Diagonal preconditioning for first order primal-dual algorithms in convex optimization, in *2011 International Conference on Computer Vision*, (Barcelona, 2011) 1762–1769.
https://doi.org/10.1109/ICCV.2011.6126441

[14] **Rockafellar, R.T.,** *Convex Analysis*, Princeton University Press, 1970.
https://doi.org/10.1515/9781400873173

[15] **Shepp, L.A. and Y. Vardi,** Maximum likelihood reconstruction for emission tomography, *IEEE Transactions on Medical Imaging*, **1** (1982) 113–122. https://doi.org/10.1109/TMI.1982.4307558

[16] **Szirmay-Kalos, L., B. Tóth, and G. Jakab,** Efficient Bregman iteration in fully 3D PET, in *2014 IEEE Nuclear Science Symposium and Medical Imaging Conference (NSS/MIC)*, (Seattle, 2014) 1–7. https://doi.org/10.1109/NSSMIC.2014.7430798

[17] **Szlávecz, Á. et al.,** GPU-based acceleration of the MLEM algorithm for SPECT parallel imaging with attenuation correction and compensation for detector response, *IFAC Proceedings Volumes*, **44** (2011) 6195–6200. https://doi.org/10.3182/20110828-6-IT-1002.02896

[18] **Vu, B.C.,** A splitting algorithm for dual monotone inclusions involving cocoercive operators, *Advances in Computational Mathematics* **38** (2013) 667–681. https://doi.org/10.1007/s10444-011-9254-8

[19] **Wang, Z., A.C. Bovik, H.R. Sheikh, and E.P. Simoncelli,** Image quality assessment: from error visibility to structural similarity, *IEEE Transactions on Image Processing* **13** (2004) 600–612. https://doi.org/10.1109/TIP.2003.819861

[20] **Zeng, G.L.,** Modification of green's one-step-late algorithm for attenuated emission data, *Biomed. Phys. Eng. Express* **5** (2019) 037001. https://dx.doi.org/10.1088/2057-1976/ab0926

Dávid Légrády
https://orcid.org/0000-0001-8678-2506
Budapest University of Technology and Economics (BME)
Institute of Nuclear Techniques
Department of Nuclear Techniques
Budapest
Hungary
david.legrady@reak.bme.hu

Ákos Rábely
https://orcid.org/0009-0000-5923-239X
Mediso Ltd.
Budapest
Hungary
akos.rabely@mediso.com

Ádám Zlehovszky
https://orcid.org/0009-0001-1896-855X
ELTE Eötvös Loránd University
Faculty of Informatics
Budapest
Hungary
adam.zlehovszky@inf.elte.hu